Article

Effects of Missing Linker Defects on the Elastic Properties and Mechanical Stability of the Metal−Organic Framework HKUST-1

Bing Wang, Penghua Ying, and Jin Zhang*

Read Online

ACCESS | Metrics & More | Article Recommendations | Supporting Information

ABSTRACT: The defects can naturally exist or be artificially designed in metal−organic frameworks (MOFs), which could significantly affect their mechanical properties. In this paper, the elastic properties of HKUST-1 with randomly distributed missing linker defects are investigated by reactive molecular dynamics simulations together with the strain-fluctuation method. Although all elastic constants of HKUST-1 are found to reduce due to the linker missing, the cubic symmetry is retained in the defective HKUST-1, indicating that the simplified Born stability criterion is still applicable in determining its mechanical stability. On the basis of the simplified Born stability criterion together with direct compression simulations, the critical pressure of instability of HKUST-1 with randomly distributed defects is found to almost linearly decrease as the defect concentration grows. The mechanical instability is similarly attributed to the compression mode in both pristine and defective HKUST-1. Moreover, the direct compression simulations indicate an obvious intermediate transition process existing during the structural collapse of the defective HKUST-1, which is absent in its pristine counterpart. Overall, this work is expected to provide a more precise understanding of the mechanical properties of realistic MOFs.
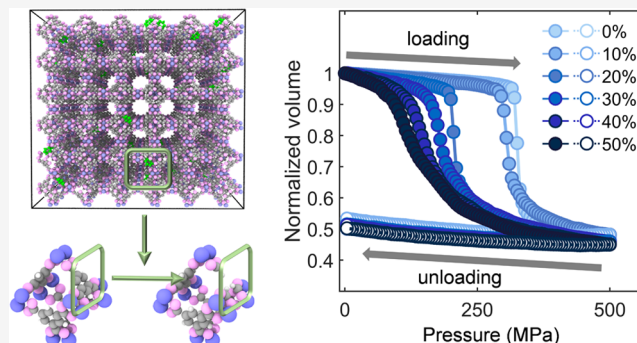
INTRODUCTION

Metal−organic frameworks (MOFs) belong to a new class of hybrid organic−inorganic materials with highly symmetrical and repetitive structures composed of metals and organic ligands.[1] The MOFs possess a good chemical and structural control as well as a superior synthetic tunability due to the modularity of their design.[2] In addition, MOF crystals usually show extremely high specific surface area,[3] high porosity,[4,5] and structural tunability.[6] Specifically, the high porosity property of most MOFs can be retained even during the adsorption and elimination of guest solvents, which makes MOFs have the potential to be used in various engineering applications such as the gas adsorption and separation, catalysis, sensing, optics, sequestration of pollutions, drug delivery, and conductive supercapacitors.[7]

It is known that defects are usually inevitable in MOFs even when the latest synthesis methods are employed.[8] In other words, most MOFs fabricated in reality contain various defects, the existence of which can greatly affect their chemical and physical properties as revealed in many existing studies.[8−10] For instance, by introducing a high density of defects in MOF-801 and adjusting the configuration of defects, the hydrophilic adsorptive behaviors of MOF can be improved.[11] Due to the combination of tricarboxylate and dicarboxylate ligands in MOF-808, MOF-808-IP and MOF-808-Pydc have less crowded Zr^{4+} sites, which results in an improved performance of the catalytic activity of MOF-808.[12] The number of

structural defects such as missing cluster defects and missing linker defects in modulated UiO-66 can be controlled precisely by selecting different synthesis and processing conditions, which can effectively increase the number of effective open metal sites and thus improve the catalytic performance of UiO-66.[13] Compared to the pristine MOF-808, its defective zirconium counterpart, i.e., d-MOF-808, can better resist the effects of strong acidic media in the postsynthesis modification process, which makes it have a higher efficiency in the application of charge transfer.[14]

As mentioned above, the defects in MOFs, on the one hand, can improve the adsorption, catalytic, and conductivity performance of MOFs. On the other hand, the defects will weaken the mechanical performance of MOFs. Very recently, through the near-field infrared nanospectroscopy experiments and density functional theory calculations, the generation mechanism of defects during the crystal growth process of MOFs (ZIF-8) and their effects on the mechanical properties of ZIF-8 were investigated.[15] It was found that the lack of
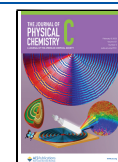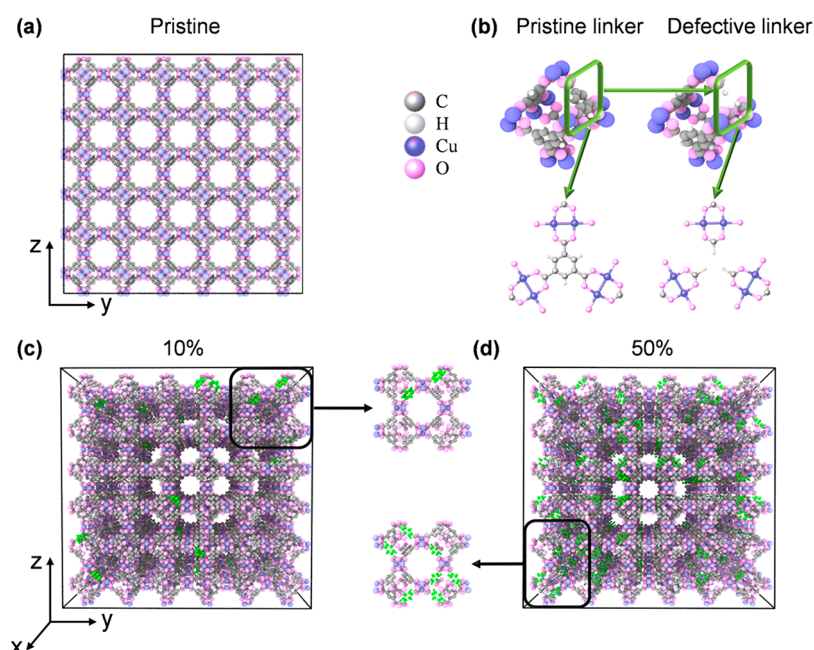
Figure 1. (a) Front view of the pristine HKUST-1 framework containing $3 \times 3 \times 3$ supercell. (b) Structures of H_3BTC organic linkers before and after linker removal. Here, three hydrogens are added to terminate each missing part. (c, d) Perspective views of $3 \times 3 \times 3$ defective HKUST-1 supercells with defect concentrations of 10% and 50%. Here, missing linkers are illustrated in green. All structures are visualized by the software OVITO.[23]

coordination bonds during the growth process is the major factor responsible for the generation of defects, which results in a lot of metal point vacancies in the synthesized ZIF-8. These metal point vacancies were found to significantly decrease the Young's modulus of defective ZIF-8. By introducing mesoporosity with different sizes in HKUST-1, the effect of mesoscopic defects on the mechanical stability of MOFs was investigated by a multiscale simulation method.[16] It was observed that in MOFs with a certain size the defects will cause a reduction in their bulk moduli. Moreover, as for MOFs possessing the same amount of defect degree or the same mesoporous void volume, MOFs with a larger cavity have a higher mechanical stability. When different types of defects exist in UiO-66 to -68 materials, a recent molecular dynamics (MD) simulation study revealed a reduction in the mechanical stability of these MOF materials, which can be affected by the distribution of defects in them.[17] A recent high-pressure powder X-ray diffraction experiment revealed the critical pressure of the onset of mechanical instability of defective UiO-66 under hydrostatic pressure.[18] A decreased bulk modulus was observed in the defective UiO-66 when compared to its pristine counterpart. However, no correlation was observed between the reduced bulk modulus and the defect concentration of UiO-66, which, to some extent, indicates the complexity of spatial integration of defects into MOFs. Overall, the above studies indicate that the presence of defects in MOFs can significantly affect their mechanical performance. Nevertheless, the correlation between the mechanical behaviors of MOFs and their defect characteristics such as the defect concentration is still not clear, which, however, is importance because the number of defects in MOFs could be variable at different growth and working environments.[19]

In this article, by taking HKUST-1 with BTC linker defects as a typical example,[20] we investigate the effect of the absence

of linker on the elastic properties of MOFs through reactive MD simulations and the strain-fluctuation method. In addition, the mechanical stability of defective HKUST-1 is comprehensively studied through direct compression simulations and the Born stability criterion. A significant effect of the missing linker defects on elastic properties and mechanical stability of HKUST-1 is found in this study. Specifically, the dependence of elastic constants and critical pressure of instability on the defect concentration of HKUST-1 is comprehensively discussed.

■ METHODOLOGY

Simulation Models. In this study, we considered the HKUST-1 having the composition the same as that first reported in experiments,[21] which is composed of Cu^{2+} as its metal center and can be noted as $[Cu_3(btc)_2]$. Specifically, as shown in Figure 1a, the considered HKUST-1 contains metal centers of Cu atoms and organic linkers of C, H, and O atoms. A $3 \times 3 \times 3$ supercell with periodic boundaries in three mutually perpendicular directions was considered in the present calculations. Thus, as shown in Figure 1a, the pristine (defect-free) HKUST-1 material has a square box configuration with 7.9 nm on each side, which totally contains 16848 atoms and 864 organic linkers (H_3BTC). To generate the HKUST-1 materials with defects in organic linkers, we followed the methods introduced in ref 20. In other words, we removed linkers randomly from the pristine HKUST-1 structure and, afterward, added three hydrogens to terminate bonds with formate as illustrated in Figure 1b.

To investigate the effect of defect concentration on the mechanical properties of HKUST-1, we considered here HKUST-1 materials having a defect concentration ranging from 0% (pristine material) to 50%. The representative structures of the generated defective HKUST-1 materials with different defect concentrations (10% and 50%) are shown

in Figure 1c,d. The green parts in the figure are the bonds that have the missing linkers. It is noted that in order to obtain more reliable mechanical properties of defective HKUST-1, we considered three randomly generated defective HKUST-1 structures for the same defect concentration, which can be realized in the defective model generation process by employing different random coefficients for the defect distribution. In this paper, these three independent defective HKUST-1 structures are named structure-1, -2, and -3. The perspectives of these three structures with different defect concentrations (10%, 25%, and 50%) are shown in Figure S1 (see the Supporting Information). Moreover, the connectivity of all defective structures was verified even for the structures with the defect concentration of 50%. The distribution of the missing linker in HKUST-1 can be quantitatively measured by a short-range order (SRO).[22] If the missing and pristine linkers as shown in Figure 1b of BTC are respectively defined as linker-A and -B, the SRO parameter α_j can be written as

$$\alpha_j = 1 - \frac{P_j^{A(B)}}{x_B} \tag{1}$$

where $P_j^{A(B)}$ denotes the conditional probability of finding linker-B at the jth neighbor site given a linker-A and x_B is the missing-linker ratio. Here, $j = 1$ was selected to identify the nearest neighbors for a given linker-A as the linkers bond to the shared Cu centers. The minimum, medium, and maximum values of SRO are −1, 0, and 1, which respectively represent the uniformly ordered, completely random, and clustered distribution of defects.[22] The SRO parameters of structure-1, -2, and -3 with defect concentrations ranging from 0 to 50% all are found to be close to 0, which denotes that the missing linker defects in three structures possess the similar completely random distribution.

Computational Methods. The mechanical behaviors of pristine and defective HKUST-1 materials considered here were investigated by MD simulations using the open-source code LAMMPS.[24] The bond breaking and creation might take place during the deformation of MOFs, which are out of the reach of classical force fields. Under this circumstance, the interactions between atoms in HKUST-1 were described by the reactive force field (ReaxFF potential) with specific parameters taken from ref 25 because the ReaxFF potential allows bond breaking and creation. The previous study has demonstrated that the ReaxFF potential can accurately describe the shearing and compressive deformation of pristine HKUST-1.[26] In addition, the ReaxFF potential also can describe the lattice structures of defective HKUST-1 because, as shown in Figure S2, the radial distribution functions and angle distribution functions of defective HKUST-1 predicted from the ReaxFF potential agree well with the results obtained from density functional theory (DFT) calculations with the Perdew−Burke−Ernzerhof (PBE) functional. Moreover, the relative energy changes of a HKUST-1 unit cell due to the absence of single missing linker obtained from ReaxFF and DFT calculations are 5.5% and 7.2%, respectively, also close to each other. Besides, a good correlation is observed between the energy changes of HKUST-1 under a finite strain perturbation obtained from ReaxFF simulations and DFT calculations (see Figure S3). This result, to some extent, indicates the reliability of the ReaxFF potential in qualitatively describing the mechanical response of HKUST-1 under loading.

In the present MD simulations, the boundary conditions of the supercell were set to be periodic, while the velocity-Verlet algorithm with a time step of 0.25 fs was used to integrate the standard Newton equations of motion. Before conducting the simulations of mechanical behaviors, a sufficient relaxation was performed to all HKUST-1 structures. To implement this structural relaxation, the energy minimization was first performed to the original HKUST-1 structures using the conjugate gradient method. Afterward, HKUST-1 structures were further relaxed at 300 K and 0 GPa in the NPT ensemble (constant number of particles, pressure, and temperature) for 50 ps and, subsequently, at 300 K in the NVT ensemble (constant number of particles, volume, and temperature) for another 50 ps. Here, the Nosé−Hoover thermostat and barostat were used to control the temperature and pressure, respectively. In addition, we chose 1000 times of time step to control the pressure and 100 times of time step to control the temperature in simulations because these parameters show the reliability in predicting the corresponding results as shown in Figure S4. It is noted that the removal of organic linkers will not cause the structural collapse of HKUST-1 after the structural relaxation, indicating the reliability of defective HKUST-1 structures constructed here. The obtained equilibrated structures were employed to calculate the elastic constants and investigate the mechanical stability of HKUST-1 at the room temperature of 300 K. Representative input files of MD simulations are available in the data repository through https://github.com/bing93wang/HKUST-1-defects.

The elastic constants of HKUST-1 were calculated by using the strain-fluctuation method in the NsT ensemble (constant numbers of particles, stress, and temperature), in which the fourth-order elastic stiffness tensor C_{ijkl} was obtained by analyzing the fluctuation of unit cell vectors:[27,28]

$$\left(\frac{K_B T}{V}\right) C_{ijkl}^{-1} = \langle \varepsilon_{ij} \varepsilon_{kl} \rangle - \langle \varepsilon_{ij} \rangle \langle \varepsilon_{kl} \rangle \tag{2}$$

where K_B is Boltzmann's constant, T is the temperature, ε_{ij} (or ε_{kl}) is the strain calculated through the method introduced in refs 27 and 28 (see details in the Supporting Information), V is the volume of the simulation cell, and C_{ijkl}^{-1} denotes the compliance tensor that is the inverse of the stiffness tensor.

It is noted that because the pristine HKUST-1 with no defects has a cubic symmetry,[29] there are only three independent elastic constants C_{1111}, C_{1122}, and C_{2323} (or C_{11}, C_{12}, and C_{44} in a Voigt notation) needed to be considered now, which are actually the moduli for the axial compression, dilation on compression, and shearing. As for the defective HKUST-1, we calculated all components of the elastic stiffness tensor to check its symmetry. Here, a structural relaxation simulation with 100 ps was first performed to make the structures reach their equilibrium. After that, another simulation with 500 ps was conducted to calculate the elastic constants. The unit cell vector was output every 10 fs. The result in Figure S4 shows the evolution of the elastic stiffness tensors with respect to simulation time, which indicates the convergency of elastic stiffness tensors after 100 ps. Therefore, in the following calculations, the data from 100 to 500 ps were selected, which was further divided into five groups. The average of compliance tensors of these five groups was treated as the final result of elastic stiffness tensors, while the standard
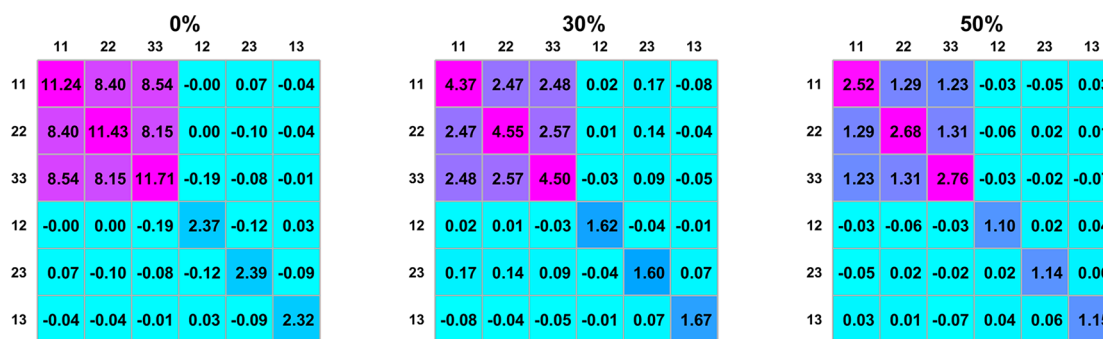
Figure 2. Elastic stiffness tensors of pristine HKUST-1 and its defective counterpart (structure-1) with the defect concentrations of 30% and 50%. The indexes "ij" and "ij" (i, j = 1, 2, and 3) of the row and column of the matrix represent the component C_{ijij} of the stiffness tensor.
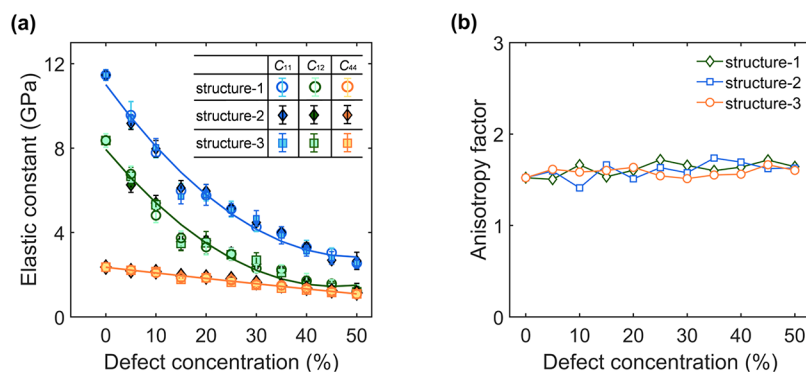

Figure 3. (a) Elastic constants C_{11}, C_{12}, and C_{44} and (b) anisotropy factor of defective HKUST-1 (structure-1, -2, and -3) with different defect concentrations. Here, lines in (a) are results of the second-order polynomial fitting of simulation results plotted to guide the eye.

deviation of the five groups of data was regarded as the calculation error.

In this paper, two computational methods including direct compression simulations and Born stability criteria[30−32] were utilized to present a comprehensive study of the mechanical instability of HKUST-1 under hydrostatic pressure. In what follows, a brief description of computation details of these methods is presented. For more details about these methods, we refer the readers to some previous papers.[33,34]

In direct compression simulations, the instability or phase transition of a system is simulated by applying the pressure on the system with a fixed loading rate, which is accompanied by changes in the volume and internal energy. In this paper, the NsT ensemble was adopted to realize the direct compression simulations at room temperature, in which the Nosé−Hoover thermostat was employed to control the pressure and temperature. Specifically, the pressure was initially fixed at 0 MPa for 250 ps to obtain the equilibrium structure. Then, the pressure increased from 0 to 500 MPa within 500 ps, corresponding to a rate of 1000 Pa/fs. This loading rate can be used to simulate the quasi-static compression of HKUST-1 because no significant difference is observed in the mechanical responses if we keep decreasing the loading rate (see Figure S6). Finally, the system was unloaded from 500 to 0 MPa at the same rate.

As for the HKUST-1 with the cubic symmetry, its mechanical stability under the hydrostatic pressure P also can be determined by the following simplified Born stability criterion[34] together with the elastic coefficients C_{11}, C_{12}, and C_{44}:

$$C_{11} + 2C_{12} + P \geq 0$$
$$C_{11} - C_{12} - 2P \geq 0$$
$$C_{44} - P \geq 0 \tag{3}$$

When one of the three criteria in eq 3 is smaller than zero, HKUST-1 with the symmetry can be identified to be instability. Here, elastic coefficients C_{11}, C_{12}, and C_{44} under different hydrostatic pressures were calculated based on the method introduced above until the instability of compressed HKUST-1 occurs.

■ RESULTS AND DISCUSSION

Elastic Properties of Defective HKUST-1. To investigate the effect of missing linker defects on the elastic properties of HKUST-1, we calculated all components of the elastic stiffness tensor of the defective HKUST-1 with a defect concentration ranging from 5% to 50% under 0 MPa in Figure S5. In general, no significant differences are observed in all three defective HKUST-1 structures considered here (structure-1, -2, and -3), which, to some extent, indicate the reliability of the present modeling and calculation methods. Thus, results of structure-1 with defect concentrations of 30% and 50% are shown as two representative examples in Figure 2, in which the result of pristine HKUST-1 is also shown here for the sake of comparison. As expected, due to its cubic symmetry, only three groups of nonzero components are found in the stiffness matrix of pristine HKUST-1, i.e., (C_{1111}, C_{2222}, C_{3333}), (C_{1122}, C_{1133}, C_{2233}), and (C_{1212}, C_{2323}, C_{2323}) because the components in each group are extremely close to each other. In other words, the elastic properties of pristine HKUST-1 indeed can be described by only three independent elastic constants of
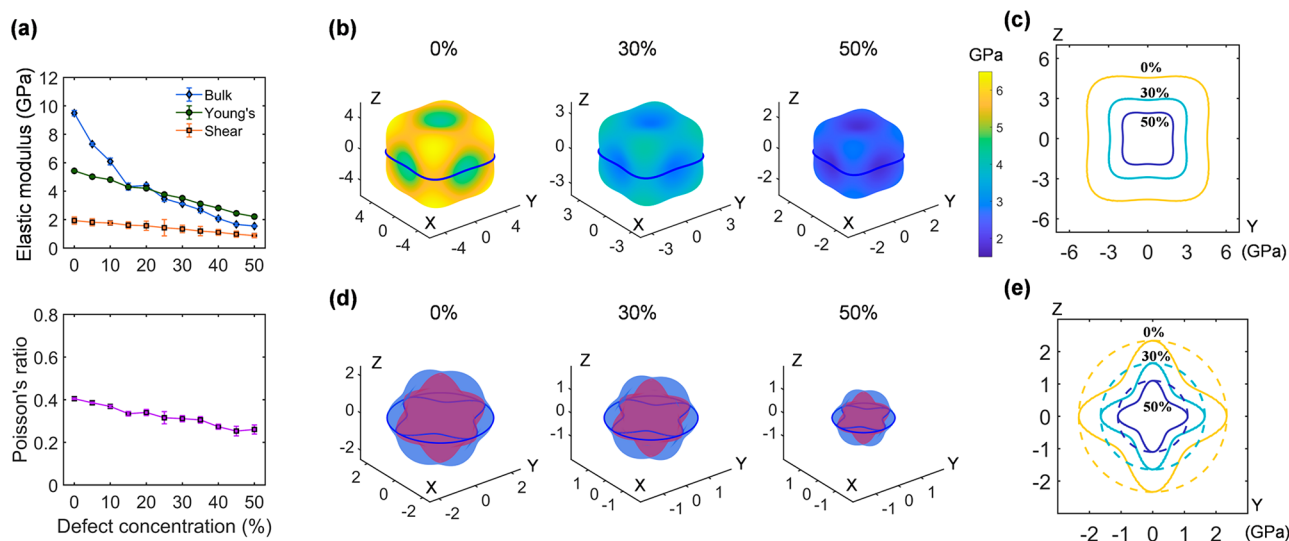
Figure 4. (a) Averaged bulk modulus K, Young's modulus E, shear modulus G, and Poisson's ratio ν of defective HKUST-1 with different defect concentrations extracted from the strain-fluctuation method. (b, c) Young's modulus of pristine HKUST-1 and its defective counterpart with defect concentrations of 30% and 50% represented in 3D spherical and 2D plane coordinates. (d, e) Shear modulus of the corresponding pristine and defective HKUST-1 represented in 3D spherical and 2D plane coordinates. The maximum and minimum values are respectively represented as blue and red surfaces in (d) and dashed and solid lines in (e).

C_{11}, C_{12}, and C_{44}, which, in this study, equal the average of all components in each group as shown below:

$$C_{11} = \frac{C_{1111} + C_{2222} + C_{3333}}{3}$$

$$C_{12} = \frac{C_{1122} + C_{1133} + C_{2233}}{3}$$

$$C_{44} = \frac{C_{1212} + C_{2323} + C_{1313}}{3} \tag{4}$$

As shown Figures 2 and S5, the stiffness matrix of all defective HKUST-1 structures is similar to that of their pristine counterpart except for a smaller value of the nonzero components of the stiffness matrix found in defective HKUST-1. The similar stiffness matrix observed in both pristine and defective HKUST-1 indicates that the cubic symmetry is retained in the defective HKUST-1 considered in this study. Thus, similar to its pristine counterpart, the elasticity of the defective HKUST-1 considered here can be well described by only the elastic constants of C_{11}, C_{12}, and C_{44}.

In order to better illustrate the effects of missing linker defects on the elastic properties of HKUST-1, in Figure 3a we graphically show the intrinsic elastic constants (C_{11}, C_{12}, and C_{44}) of the defective HKUST-1 (structure-1, -2, and -3) with different defect concentrations. It is found that all elastic constants decrease as the defect concentration increases. Specifically, when the concentration of randomly distributed defects grows from 0 to 50%, C_{11}, C_{12}, and C_{44} are found to reduce by 82%, 90%, and 58%, respectively. In other words, when compared with C_{44}, C_{11}, and C_{12} of HKUST-1 are more sensitive to the amount of missing linker defects, which indicates that the effect of missing linker defects on the shrinkage deformation of defective HKUST-1 is larger than that on its shearing deformation. On the basis of the elastic constants shown in Figure 3a, we further evaluated the anisotropy of defective HKUST-1 with different defect concentrations. Because the cubic symmetry is retained in the defective HKUST-1, the Zener anisotropy index $A = 2C_{44}/$

($C_{11} - C_{12}$) was employed here to measure the anisotropy.[35] As shown in Figure 3b, the Zener anisotropy index keeps around 1.6 for all defective HKUST-1 materials, which is also extremely close to the value of the pristine HKUST-1. This result proves that the pristine and defective HKUST-1 materials hold the similar mechanical anisotropy.

Based on the Voigt−Reuss−Hill model,[36−38] C_{11}, C_{12}, and C_{44} of HKUST-1 extracted from the strain-fluctuation method can be adopted to predict the bulk modulus K, shear modulus G, Young's modulus E, and Poisson's ratio ν through

$$K = \frac{C_{11} + 2C_{12}}{3}, \quad G = \frac{3C_{44} + C_{11} - C_{12}}{5},$$

$$E = \frac{9KG}{3K + G}, \quad \nu = \frac{E}{2G} - 1 \tag{5}$$

We compared the Young's modulus and bulk modulus of pristine HKUST-1 obtained from the present ReaxFF MD simulations to the results reported in previous experiments or simulations (see Table S1) to verify the accuracy of the present simulations. In general, the Young's modulus obtained here well agrees with the results reported in previous nano-indentation experiments of {100}-faceted HKUST-1 crystals at room temperature.[39] The values of K and E obtained here are smaller than the results obtained in the previous density functional theory calculations at absolute zero.[40] The larger temperature employed here accounts for the smaller K and E obtained in this study due to the thermally induced softening effect.[39] In Figure 4a, K, G, E, and ν of HKUST-1 possessing different defect concentrations are further shown, which are values averaged over different directions. As expected, all elastic moduli (K, G, and E) are found to decrease as the defect concentration increases and the reduction of G is smaller than that of other two elastic moduli (K and E). For example, when the defect concentration increases from 0 to 50%, K, E, and G respectively decrease from 9.43 ± 0.347, 5.33 ± 0.154, and 1.90 ± 0.0057 GPa to 1.51 ± 0.097, 2.17 ± 0.100, and 0.86 ± 0.045 GPa. Similar to the elastic moduli, a significant effect of missing linker defects on the Poisson's ratio ν is also found, as
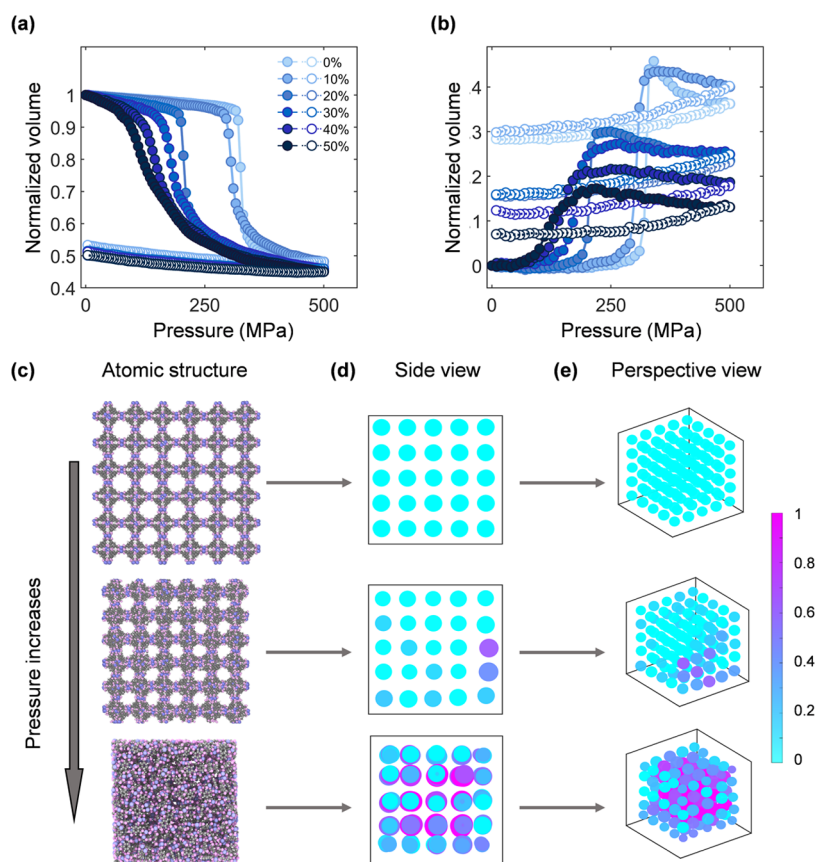
Figure 5. (a, b) Evolution of normalized volume and internal energy change of pristine and defective HKUST-1 during the loading and unloading processes in direct compression simulations. Here, the closed circles (●) and open circles (○) represent the results in the loading and unloading processes, respectively. (c) Representative atomic structures of pristine HKUST-1 during the loading process in direct compression simulations. (d, e) Side and perspective views of the relative volume change of the local atomic frame constructed by the component Cu atoms in the same pore.

shown in Figure 4a. We provide specific data in Table S2. For example, in the similar growth process of defect concentration, ν is found to reduce by 40%. To further reveal the effects of missing linker defects on the overall elastic properties of HKUST-1, in Figure 4b−e we show the spatial dependence of the Young's modulus and shear modulus of pristine HKUST-1 (with a defect concentration of 0%) and defective HKUST-1 with defect concentrations of 30% and 50% in three-dimensional (3D) spherical and two-dimensional (2D) plane coordinates. Specifically, because the shear modulus is a function of two unit vectors, we show here both its maximal and minimal values.[41,42] Generally, the Young's modulus and shear modulus in all directions are found to synchronously decrease as the defect concentration increases. In other words, despite the quantitative difference between them, the elastic moduli in pristine and defective HKUST-1 almost have the same distribution, which is ascribed to the same cubic symmetry existing in both pristine and defective HKUST-1.

Mechanical Instability of Defective HKUST-1. We first investigate the mechanical responses of pristine and defective HKUST-1 under compression by using direct compression simulations. The changes in the normalized volume and normalized internal energy of pristine and defective HKUST-1 during the loading and unloading processes are shown in Figures 5a and 5b, respectively. Here, the normalized volume is defined as the ratio of the volume of compressed HKUST-1 to its initial volume without compression. As for the pristine HKUST-1 without defects, its volume is found to monotoni-

cally decrease with increasing pressure at the initial stage of loading process, indicating its shrinkage without change in the crystal structure. When the pressure increases from 321 to 325 MPa, a sudden drop of normalized volume dramatically from 0.95 to 0.59 is observed, which leads to a sharp increase of the energy change of each atom in the system as shown in Figure 5b. A similar sudden volume drop was also observed in very recent *in situ* compression experiments of HKUST-1 micro-pillars.[43] The abrupt volume and energy changes signify the onset of the mechanical instability or the global collapse of the entire HKUST-1 structure. This structural collapse results in the transformation of HKUST-1 form a porous structure with the open-pore configuration to a dense structure with the closed-pore configuration through an intermediate state as shown in Figure 5c. Specifically, this closed-pore structure after the structural collapse will not recover to the initial open-pore structure even after the pressure is completely released. Similar unrecoverable plastic deformations in compressed HKUST-1 were also observed in the recent experiment.[43]

We also calculated the relative volume change of the local atomic frame constructed by the component Cu atoms in the same pore of HKUST-1, which is quantitatively represented by different colors and sizes of circles in Figure 5d,e. This quantitative representation of volume change of atomic frames can be utilized to characterize the local structural evolution of HKUST-1 during direct compression simulations. It is obviously found that the global collapse of the entire structure
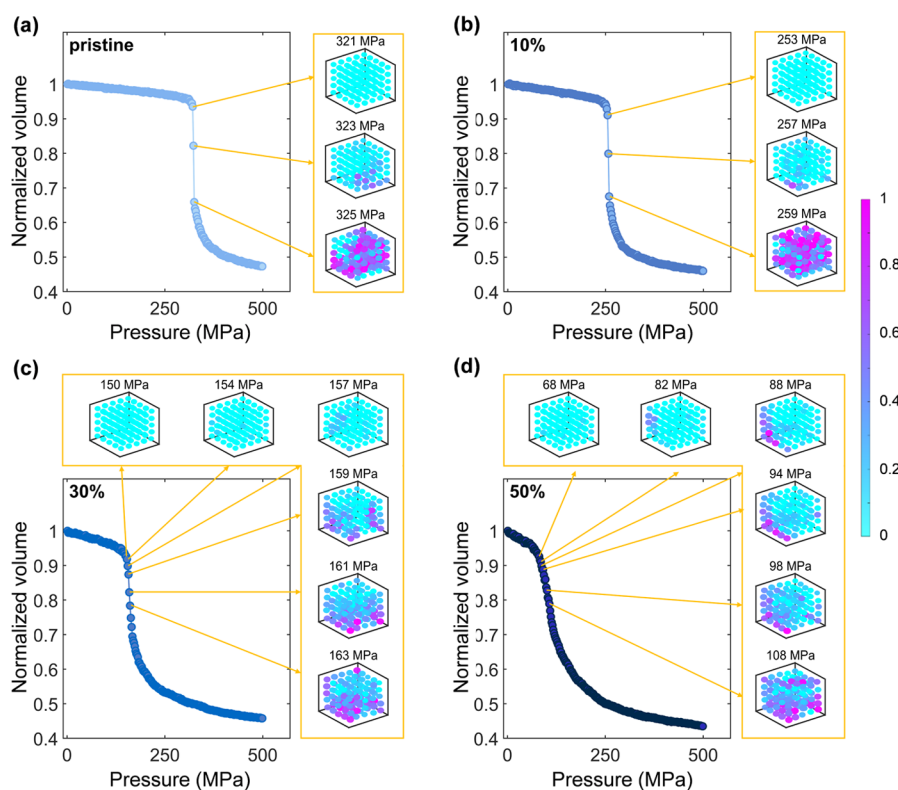
Figure 6. Local structural evolution of (a) pristine HKUST-1 and its defective counterpart with defect concentrations of (b) 10%, (c) 30%, and (d) 50% during the intermediate transition process.
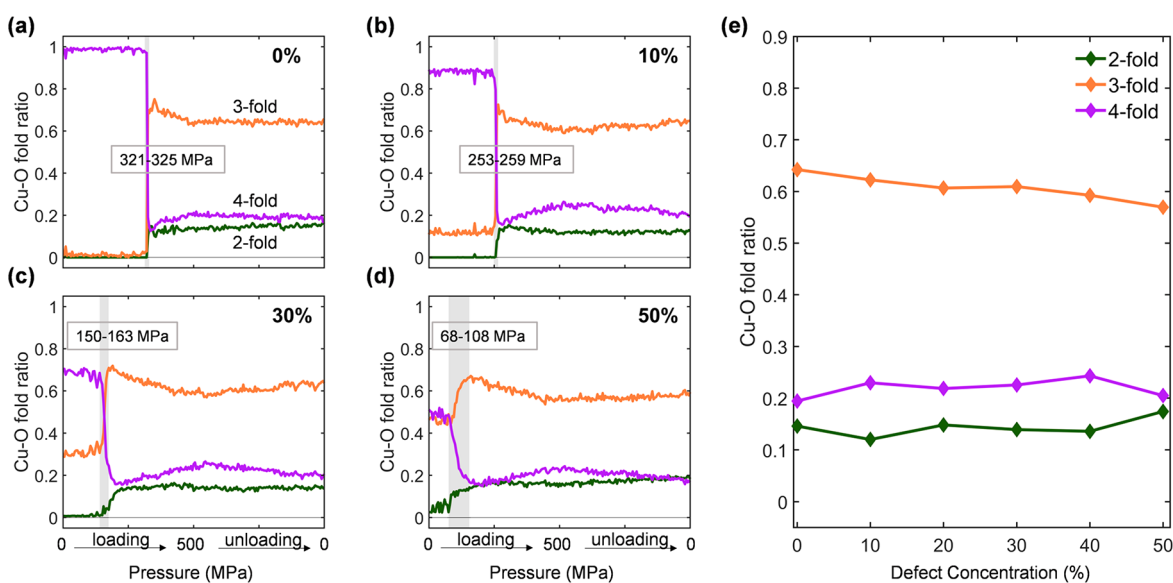

Figure 7. (a−d) Evolution of the percentage of Cu−O coordination numbers of pristine HKUST-1 and its defective counterpart with defect concentrations of 10%, 30%, and 50% during the whole direct compression simulation process. (e) Average percentage of Cu−O coordination numbers after structural collapse. A distance criterion of 2.5 Å was employed here as the threshold for coordination.

of pristine HKUST-1 is induced by the dramatic shrinkage of almost all local pores in HKUST-1.

A similar mechanical instability behavior is observed in the defective HKUST-1 structures except for a smaller critical pressure of instability is observed in them. The reduction of the critical pressure becomes significant as the defect concentration grows. For example, the critical pressure decreases from 283 MPa of HKUST-1 with a small defect concentration of 5% to 76 MPa of its counterpart with a relatively large defect concentration of 50%. From Figure 5a we also see that when the defect concentration is smaller than 20%, there is no obvious intermediate transition process during the collapse of defective HKUST-1. As shown in Figure 6a,b, the abrupt drop of the volume in this process is induced by the dramatic and almost synchronous shrinkage of all pores in HKUST-1, which is similar to the phenomenon observed in the pristine HKUST-1. However, when the defect concentration becomes larger than 20%, an intermediate process is
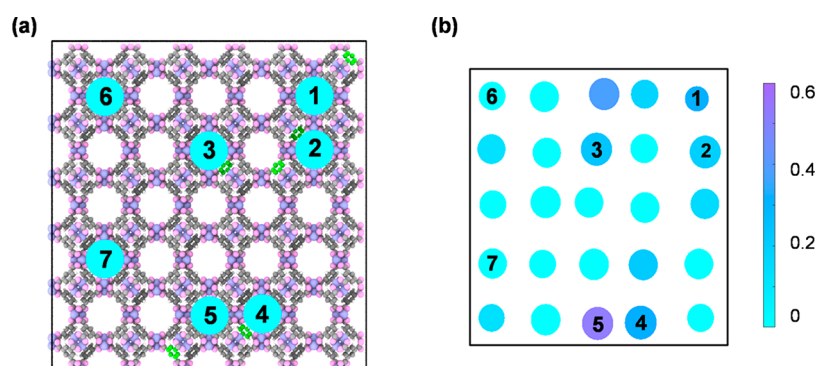
Figure 8. Cross-sectional view of (a) HKUST-1 with a defect concentration of 10% and (b) the size change of its pores under the pressure of 253 MPa.

apparently observed during the transition from the initial open-pore configuration to the final closed-pore configuration as shown in Figure 6c,d. The apparent intermediate transition process during the collapse of these HKUST-1 structures is due to the significantly asynchronous shrinkage of their local pores. Moreover, the asynchronization of volume change of these defective HKUST-1 materials becomes more aggressive as the defect concentration grows, which can result in the extension of the intermediate transition process. For example, as shown in Figure 6c, the transition of the entire HKUST-1 with a defect concentration of 30% from the open-pore configuration to closed-pore configuration starts at 150 MPa and finishes at 163 MPa, corresponding to a duration of 13 MPa. As for the defective HKUST-1 with a larger defect concentration of 50%, the onset and end of the transition process are found at 68 and 108 MPa, respectively, resulting in an extension of the duration of this intermediate transition process to 40 MPa, as shown in Figure 6d. The reliability of the results about the intermediate state has also been verified by the method of pressure versus volume equations of state ($P–V$ EOS),[28] in which the compression simulations were implemented by gradually decreasing the volume of HKUST-1. Here, a relaxation simulation with 200 ps was applied to each step during the volume change. According to the $P–V$ EOS shown in Figure S7a, an intermediate state indeed exists in the defective HKUST-1, which, however, is not observed in its pristine counterpart. Moreover, the potential energy of HKUST-1 at the intermediate state keeps stable during the relaxation simulation of each volume change step (see Figure S7b), which indicates the structural stability of HKUST-1 at the intermediate state.

In Figure 7 we illustrate the evolution of the percentage of Cu−O coordination numbers[43] (discrete values of 2, 3, and 4) during the direct compression simulations. As shown in Figure 7a–d, an abrupt drop of the 4-fold coordination is observed at the critical pressure of instability, resulting in the significant increase of 2- and/or 3-fold coordination. Such change in the percentage of the Cu−O coordination numbers indicates the destruction of some Cu−O coordination bonds during the structural collapse process. Moreover, almost no significant changes are observed in the percentage of Cu−O coordination numbers during the unloading process, which indicates that almost no new Cu−O coordination bonds are created in this process. In other words, the HKUST-1 retains the closed-pore configuration and cannot recover to its original open-pore configuration even after the compression is completely

released, which is consistent with the result directly extracted from direct compression simulations as shown in Figure 6.

It is also observed that the percentage of 4-fold Cu−O coordination bonds in original HKUST-1 structures without compression decreases with the increase of defect concentration. Specially, when the defect concentration is up to 50%, the percentage of 4-fold coordination becomes the smallest. The lack of Cu−O coordination bonds in defective HKUST-1 will decrease its general structural stiffness, which results in a smaller elastic modulus in the defective HKUST-1 with a lager defect concentration as observed above. In the closed-pore configuration of HKUST-1 after collapse, as shown in Figure 7e, the percentage of Cu−O coordination numbers is almost independent of the defect concentration, indicating the independence of the elastic modulus of HKUST-1 after collapse. We also considered the pristine HKUST-1 inversely under a tension or a negative pressure after the complete unloading. In Figure S8a, we show the structure of HKUST-1 with the negative pressure of 340 MPa. Although the volume of this structure recovers to its initial value, it cannot recover to its original regular porous structure. As shown in Figure S8b, there are almost no new Cu−O coordination bonds created in this tension process, indicating that the destruction of Cu−O coordination bonds or the plasticity of HKUST-1 after the structural collapse is irreversible even if a negative pressure is applied.

If the missing linker defect is equivalently treated as a void, the stress concentration phenomenon may be induced nearby, which can promote the destruction of Cu−O coordination bonds nearby and thus result in a smaller critical pressure of instability. To prove this deduction, we show in Figure 8 the cross-sectional view of the size change in pores in the HKUST-1 with a defect concentration of 10% under the compression near the critical pressure of instability. As can be seen from the figure, detective changes are found in the size of the most pores containing missing linker defects (see pores 1−5). In contrast, the pores that not involve any missing linker defects, e.g., pores 6 and 7, are found to exhibit no significant changes in their size. Thus, the gradual accumulation process of destruction of Cu−O coordination bonds in the defective HKUST-1 with a large defect concentration fundamentally results in the apparent intermediate process and the gradual volume change during the collapse of defective HKUST-1.

Because the so-called structural collapse or the mechanical instability can topologically change the crystal structure of HKUST-1, it is thus expected that the missing linker defects should have different effects on the mechanical properties of
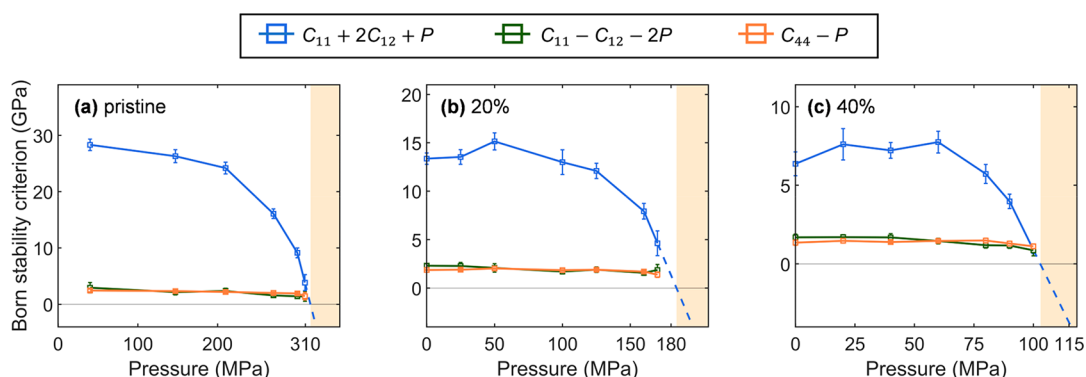
Figure 9. Born stability criteria of (a) pristine HKUST-1, (b) defective HKUST-1 with a defect concentration of 20%, and (c) defective HKUST-1 with a defect concentration of 40% under different pressures.

HKUST-1 prior to and after collapse. Here, magnitudes of bulk modulus of HKUST-1 prior to and after collapse were evaluated from the inverse to the slope of $V-P$ curves shown in Figure 5a because the bulk modulus K can be related to the relative change in volume V at different applied pressures P, i.e., $K = -V\partial P/\partial V$. Prior to the structural collapse, a larger slope is observed in $V-P$ curves of the defective HKUST-1 with a larger defect concentration, which indicates that the bulk modulus of HKUST-1 with open-pore configuration reduces as the defect concentration increases. This finding is consistent with the result directly extracted from the above strain-fluctuation method (see Figure 4a). However, after the complete collapse of HKUST-1, $V-P$ curves of pristine HKUST-1 and defective HKUST-1 with different defect concentrations are found to almost overlap with each other, indicating that missing linker defects almost have no effects on the bulk modulus of HKUST-1 with closed-pore configuration after collapse. This result can be further proven by the almost overlapped $V-P$ curves of all defective HKUST-1 materials during the unloading process, as shown in Figure 5a. This defect-independent bulk modulus observed here is consistent with the result deduced above from the Cu−O coordination numbers.

In the above discussion, we have proven that HKUST-1 can retain the cubic symmetry even when it contains the randomly distributed missing linker defects as considered in this study. Under this circumstance, the simplified Born stability criterion, i.e., eq 3, is still applicable for defective HKUST-1. Thus, the critical pressure of instability of both pristine and defective HKUST-1 materials as well as their instability mode is further investigated by the Born stability criterion together with the elastic constants. In doing this, the elastic constants (C_{11}, C_{12}, and C_{44}) of HKUST-1 under different hydrostatic pressures were calculated until the structure becomes unstable. In Figure 9, we show the evolution of three Born stability criteria of pristine and defective HKUST-1 with increasing pressure. As the representative examples of defective HKUST-1, only results of defective HKUST-1 materials with defect concentrations of 20% and 40% are shown here. The results of some other defective HKUST-1 materials with structure-1, -2, and -3 are shown in Figures S9 and S10. The critical pressure of instability corresponds to the smallest extrapolated value among three independent Born stability criteria shown in Figure 9, which represent three instability deformation modes. As in Figures 9 and S9, $C_{11} + 2C_{12} + P$ is the primary criterion determining the mechanical instability of pristine HKUST-1; this result indicates that the mechanical instability

of both pristine and defective HKUST-1 is induced by the shrinkage deformation instead of shearing deformation observed in some other MOFs such as ZIF-8.[45,46]

In Figure 10 we show the critical pressure of instability of HKUST-1 with different defect concentrations obtained from
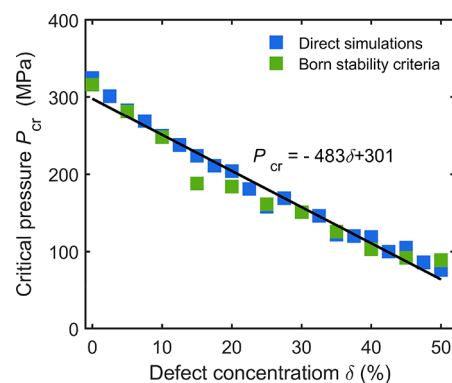

Figure 10. Critical pressures of instability of HKUST-1 with different defect concentrations obtained from direct compression simulations and the Born stability criterion method.

the above two methods including direct compression simulations and Born stability criteria. A more detailed comparison between these two methods can be found in Table S3. Overall, as shown in Figure 9 and Table S3, results obtained from two independent methods are consistent with each other, which not only proves the accuracy of the obtained critical pressures but also indicates the applicability of simplified Born stability criteria of eq 3 in determining the mechanical instability of the defective HKUST-1 considered here. Moreover, we also find in Figure 10 that the critical pressure of instability nearly decreases linearly with growing defect concentration, indicating that the HKUST-1 possessing more defects exhibits a less mechanical stability. Specifically, the critical pressure decreases from 316 to 89 MPa when the defect concentration increases from 0 (pristine HKUST-1) to 50%. After applying the linear curve fitting to the simulation results shown in Figure 10 we show in this figure a predictive equation for the critical pressures P_{cr} of HKUST-1 with different defect concentrations δ, which can be applied to predict the critical pressure of HKUST-1 with randomly distributed missing linker defects.

CONCLUSIONS

In this paper, the elastic constants of HKUST-1 containing randomly distributed missing linker defects are evaluated through ReaxFF MD simulations together with the strain-fluctuation method. It is found that all elastic constants of HKUST-1 (C_{11}, C_{12}, and C_{44}) decrease as the defect concentration grows assuming the defects to be distributed randomly, which is especially more evident for C_{11} and C_{12}, indicating the more significant influence of missing linker defects on the shrinkage deformation of HKUST-1 compared to that on the shearing deformation. Despite the reduction in elastic constants, the defective HKUST-1 is found to hold the cubic symmetry, which indicates the applicability of simplified Born stability criteria in determining its mechanical stability. Thus, the effect of missing linker defects on the mechanical instability of defective HKUST-1 is examined through the simplified Born stability criteria as well as direct compression simulations. The critical pressure of instability of the present defective HKUST-1 with randomly distributed missing linker defects is found to linearly decrease as the defect concentration grows. Meanwhile, an obvious intermediate transition process uniquely exists in the structural collapse process of defective HKUST-1 materials, which is attributed to the asynchronous shrinkage of their local pores.

This work is expected to not only expand current knowledge of mechanical properties of defective MOFs but also provide an important guideline for applications of realistic MOFs. On the other hand, it is worth pointing out that this study only considers the defective MOFs with missing linker defects. Actually, besides missing linker defects, some other defects such as the missing cluster defects may also exist during the self-assembly of MOFs.[22,47] A detailed comparison among effects of different types of defects on the mechanical properties of MOFs deserves a comprehensive study in the future. Besides, although the present ReaxFF potential is reliable to present a qualitative description of the response of HKUST-1 under mechanical loading, there exist some quantitative differences between ReaxFF and DFT results (see Figure S3). Thus, some force fields with a higher precision such as the machine learning potential[48] is still desirable to be developed in the near future to give a more quantitatively precise prediction of the mechanical behaviors of HKUST-1.

ASSOCIATED CONTENT

Ⓢ Supporting Information

The Supporting Information is available free of charge at https://pubs.acs.org/doi/10.1021/acs.jpcc.2c06954.

> Comparison between the Reaxff potential in MD simulations and PBE functional in DFT calculations for HKUST-1, validation and convergence studies of the calculated elastic constants, detailed results of elastic constants of three considered structures, and the definition of the strain used in the strain-fluctuation method (PDF)

AUTHOR INFORMATION

Corresponding Author

Jin Zhang − *School of Science, Harbin Institute of Technology, Shenzhen 518055, P. R. China;* ⓘ orcid.org/0000-0002-7032-4399; Email: jinzhang@hit.edu.cn

Authors

Bing Wang − *School of Science, Harbin Institute of Technology, Shenzhen 518055, P. R. China*

Penghua Ying − *School of Science, Harbin Institute of Technology, Shenzhen 518055, P. R. China*

Complete contact information is available at:
https://pubs.acs.org/10.1021/acs.jpcc.2c06954

Author Contributions

B.W. and P.Y. contributed equally to this work.

Notes

The authors declare no competing financial interest.

ACKNOWLEDGMENTS

REFERENCES

(1) Eddaoudi, M.; Kim, J.; Rosi, N.; Vodak, D.; Wachter, J.; O'Keeffe, M.; Yaghi, O. M. Systematic Design of Pore Size and Functionality in Isoreticular MOFs and Their Application in Methane Storage. *Science* **2002**, *295*, 469−472.

(2) Baumann, A. E.; Burns, D. A.; Liu, B.; Thoi, V. S. Metal-Organic Framework Functionalization and Design Strategies for Advanced Electrochemical Energy Storage Devices. *Commun. Chem.* **2019**, *2*, 1−14.

(3) Biserčić, M. S.; Marjanović, B.; Zasońska, B. A.; Stojadinović, S.; Ćirić-Marjanović, G. Novel Microporous Composites of MOF-5 and Polyaniline with High Specific Surface Area. *Synth. Met.* **2020**, *262*, 116348.

(4) Schneider, C.; Ukaj, D.; Koerver, R.; Talin, A. A.; Kieslich, G.; Pujari, S. P.; Zuilhof, H.; Janek, J.; Allendorf, M. D.; Fischer, R. A. High Electrical Conductivity and High Porosity in a Guest@MOF Material: Evidence of TCNQ Ordering within Cu_3BTC_2 Micropores. *Chem. Sci.* **2018**, *9*, 7405−7412.

(5) Xiang, S.; Huang, J.; Li, L.; Zhang, J.; Jiang, L.; Kuang, X.; Su, C.-Y. Nanotubular Metal−Organic Frameworks with High Porosity Based on T-Shaped Pyridyl Dicarboxylate Ligands. *Inorg. Chem.* **2011**, *50*, 1743−1748.

(6) Gadipelli, S.; Guo, Z. Postsynthesis Annealing of MOF-5 Remarkably Enhances the Framework Structural Stability and CO_2 Uptake. *Chem. Mater.* **2014**, *26*, 6333−6338.

(7) Yap, M. H.; Fow, K. L.; Chen, G. Z. Synthesis and Applications of MOF-Derived Porous Nanostructures. *Green energy environ.* **2017**, *2*, 218−245.

(8) Sholl, D. S.; Lively, R. P. Defects in Metal-Organic Frameworks: Challenge or Opportunity? *J. Phys. Chem. Lett.* **2015**, *6*, 3437−3444.

(9) Dissegna, S.; Epp, K.; Heinz, W. R.; Kieslich, G.; Fischer, R. A. Defective Metal-Organic Frameworks. *Adv. Mater.* **2018**, *30*, 1704501.

(10) Bennett, T. D.; Cheetham, A. K.; Fuchs, A. H.; Coudert, F.-X. Interplay between Defects, Disorder and Flexibility in Metal-Organic Frameworks. *Nat. Chem.* **2017**, *9*, 11−16.

(11) Choi, J.; Lin, L.-C.; Grossman, J. C. Role of Structural Defects in the Water Adsorption Properties of MOF-801. *J. Phys. Chem. C Nanomater. Interfaces* **2018**, *122*, 5545−5552.

(12) Mautschke, H.-H.; Drache, F.; Senkovska, I.; Kaskel, S.; Llabrés, I.; Xamena, F. X. Catalytic Properties of Pristine and Defect-Engineered.MOF-808 Metal Organic Frameworks. *Catal. Sci. Technol.* **2018**, *8*, 3610−3616.

(13) Wang, J.; Liu, L.; Chen, C.; Dong, X.; Wang, Q.; Alfilfil, L.; AlAlouni, M. R.; Yao, K.; Huang, J.; Zhang, D.; Han, Y. Engineering Effective Structural Defects of Metal−Organic Frameworks to

Enhance Their Catalytic Performances. *J. Mater. Chem. A Mater. Energy Sustain.* **2020**, *8*, 4464−4472.

(14) Ferhi, N.; Desalegn Assresahegn, B.; Ardila-Suarez, C.; Dissem, N.; Guay, D.; Duong, A. Defective Metal−Organic Framework-808@ polyaniline Composite Materials for High Capacitance Retention Supercapacitor Electrodes. *ACS Appl. Energy Mater.* **2022**, *5*, 1235−1243.

(15) Möslein, A. F.; Donà, L.; Civalleri, B.; Tan, J.-C. Defect Engineering in Metal−Organic Framework Nanocrystals: Implications for Mechanical Properties and Performance. *ACS Appl. Nano Mater.* **2022**, *5*, 6398−6409.

(16) Dürholt, J. P.; Keupp, J.; Schmid, A. R. The Impact of Mesopores on the Mechanical Stability of HKUST-1: A Multiscale Investigation. *Eur. J. Inorg. Chem.* **2016**, *27*, 4517−4523.

(17) Rogge, S. M. J.; Wieme, J.; Vanduyfhuys, L.; Vandenbrande, S.; Maurin, G.; Verstraelen, T.; Waroquier, M.; Van Speybroeck, V. Thermodynamic Insight in the High-Pressure Behavior of UiO-66: Effect of Linker Defects and Linker Expansion. *Chem. Mater.* **2016**, *28*, 5721−5732.

(18) Dissegna, S.; Vervoorts, P.; Hobday, C. L.; Düren, T.; Daisenberger, D.; Smith, A. J.; Fischer, R. A.; Kieslich, G. Tuning the Mechanical Response of Metal−Organic Frameworks by Defect Engineering. *J. Am. Chem. Soc.* **2018**, *140*, 11581−11584.

(19) Chaemchuen, S.; Luo, Z.; Zhou, K.; Mousavi, B.; Phatanasri, S.; Jaroniec, M.; Verpoort, F. Defect Formation in Metal−Organic Frameworks Initiated by the Crystal Growth-Rate and Effect on Catalytic Performance. *J. Catal.* **2017**, *354*, 84−91.

(20) Islamov, M.; Babaei, H.; Wilmer, C. E. Influence of Missing Linker Defects on the Thermal Conductivity of Metal-Organic Framework HKUST-1. *ACS Appl. Mater. Interfaces* **2020**, *12*, 56172−56177.

(21) Chui, S. S.-Y.; Lo, S. M.-F.; Charmant, J. P. H.; Orpen, A. G.; Williams, I. D. A Chemically Functionalizable Nanoporous Material $[Cu_3(TMA)_2 (H_2O)_3]_n$. *Science* **1999**, *283*, 1148−1150.

(22) Wu, Y.; Duan, H.; Xi, H. Machine Learning-Driven Insights into Defects of Zirconium Metal−Organic Frameworks for Enhanced Ethane−Ethylene Separation. *Chem. Mater.* **2020**, *32*, 2986−2997.

(23) Stukowski, A. Visualization and Analysis of Atomistic Simulation Data with OVITO - the Open Visualization Tool Modelling Simul. *Mater. Sci. Eng.* **2010**, *18*, 015012.

(24) Thompson, A. P.; Aktulga, H. M.; Berger, R.; Bolintineanu, D. S.; Brown, W. M.; Crozier, P. S.; in 't Veld, P. J.; Kohlmeyer, A.; Moore, S. G.; Nguyen, T. D.; Shan, R.; Stevens, M. J.; Tranchida, J.; Trott, C.; Plimpton, S. J. LAMMPS - a Flexible Simulation Tool for Particle-Based Materials Modeling at the Atomic, Meso, and Continuum Scales. *Comput. Phys. Commun.* **2022**, *271*, 108171.

(25) Monti, S.; Li, C.; Carravetta, V. Reactive Dynamics Simulation of Monolayer and Multilayer Adsorption of Glycine on Cu (110). *J. Phys. Chem. C* **2013**, *117*, 5221−5228.

(26) Mohamed, S. A.; Kim, J. Gas Adsorption Enhancement in Partially Amorphized Metal−Organic Frameworks. *J. Phys. Chem. C* **2021**, *125*, 4509−4518.

(27) Parrinello, M.; Rahman, A. Strain Fluctuations and Elastic Constants. *J. Chem. Phys.* **1982**, *76*, 2662−2666.

(28) Rogge, S. M. J.; Waroquier, M.; Van Speybroeck, V. Reliably Modeling the Mechanical Stability of Rigid and Flexible Metal−Organic Frameworks. *Acc. Chem. Res.* **2018**, *51*, 138−148.

(29) Ryder, M. R.; Civalleri, B.; Cinque, G.; Tan, J.-C. Discovering Connections between Terahertz Vibrations and Elasticity Underpinning the Collective Dynamics of the HKUST-1 Metal−Organic Framework. *CrystEngComm.* **2016**, *18*, 4303−4312.

(30) Born, M. On the Stability of Crystal Lattices. *I. Math. proc. Camb. Philos. Soc.* **1940**, *36*, 160−172.

(31) Rogge, S. M. J.; Vanduyfhuys, L.; Ghysels, A.; Waroquier, M.; Verstraelen, T.; Maurin, G.; Van Speybroeck, V. A Comparison of Barostats for the Mechanical Characterization of Metal-Organic Frameworks. *J. Chem. Theory. Comput.* **2015**, *11*, 5583−5597.

(32) Vanduyfhuys, L.; Rogge, S. M. J.; Wieme, J.; Vandenbrande, S.; Maurin, G.; Waroquier, M.; Van Speybroeck, V. Thermodynamic Insight into Stimuli-Responsive Behaviour of Soft Porous Crystals. *Nat. Commun.* **2018**, *9*, 204.

(33) Ying, P.; Zhang, J.; Zhong, Z. Pressure-Induced Phase Transition of Isoreticular MOFs: Mechanical Instability Due to Ligand Buckling. *Microporous Mesoporous Mater.* **2021**, *312*, 110765.

(34) Morris, J. W., Jr.; Krenn, C. R. The Internal Stability of an Elastic Solid. *Philos. Mag. A* **2000**, *80*, 2827−2840.

(35) Lau, K.; McCurdy, A. K. Elastic Anisotropy Factors for Orthorhombic, Tetragonal, and Hexagonal Crystals. *Phys. Rev. B Condens. Matter* **1998**, *58*, 8980−8984.

(36) Voigt, W. *Lehrbuch der Kristallphysik*; Vieweg & Teubner Verlag Press: 1928.

(37) Reuss, A. Berechnung der Fließgrenze von Mischkristallen auf Grund der Plastizitätsbedingung für Einkristalle. *Z. Angew. Math. Mech.* **1929**, *9*, 49−58.

(38) Hill, R. The Elastic Behaviour of a Crystalline Aggregate. *Proc. Phys. Soc.* **1952**, *65*, 349−354.

(39) Heinen, J.; Ready, A. D.; Bennett, T. D.; Dubbeldam, D.; Friddle, R. W.; Burtch, N. C. Elucidating the Variable-Temperature Mechanical Properties of a Negative Thermal Expansion Metal−Organic Framework. *ACS Appl. Mater. Interfaces* **2018**, *10*, 21079−21083.

(40) Bundschuh, S.; Kraft, O.; Arslan, H. K.; Gliemann, H.; Weidler, P. G.; Wöll, C. Mechanical Properties of Metal-Organic Frameworks: An Indentation Study on Epitaxial Thin Films. *Appl. Phys. Lett.* **2012**, *101*, 101910.

(41) Marmier, A.; Lethbridge, Z. A. D.; Walton, R. I.; Smith, C. W.; Parker, S. C.; Evans, K. E. ElAM: A Computer Program for the Analysis and Representation of Anisotropic Elastic Properties. *Comput. Phys. Commun.* **2010**, *181*, 2102−2115.

(42) Gaillac, R.; Pullumbi, P.; Coudert, F.-X. ELATE: An Open-Source Online Application for Analysis and Visualization of Elastic Tensors. *J. Phys.: Condens. Matter* **2016**, *28*, 275201.

(43) Zeng, Z.; Xiao, Y.; Wheeler, J. W.; Tan, J.-C. In Situ Micropillar Compression of an Anisotropic Metal-Organic Framework Single Crystal, 2022.

(44) Gaillac, R.; Pullumbi, P.; Bennett, T. D.; Coudert, F.-X. Structure of Metal−Organic Framework Glasses by *Ab Initio* Molecular Dynamics. *Chem. Mater.* **2020**, *32* (18), 8004−8011.

(45) Hegde, V. I.; Tan, J.-C.; Waghmare, U. V.; Cheetham, A. K. Stacking Faults and Mechanical Behavior beyond the Elastic Limit of an Imidazole-Based Metal Organic Framework: ZIF-8. *J. Phys. Chem. Lett.* **2013**, *4*, 3377−3381.

(46) Ortiz, A. U.; Boutin, A.; Fuchs, A. H.; Coudert, F.-X. Investigating the Pressure-Induced Amorphization of Zeolitic Imidazolate Framework ZIF-8: Mechanical Instability Due to Shear Mode Softening. *J. Phys. Chem. Lett.* **2013**, *4*, 1861−1865.

(47) Feng, L.; Yuan, S.; Zhang, L.-L.; Tan, K.; Li, J.-L.; Kirchon, A.; Liu, L.-M.; Zhang, P.; Han, Y.; Chabal, Y. J.; Zhou, H.-C. Creating Hierarchical Pores by Controlled Linker Thermolysis in Multivariate Metal -Organic Frameworks. *J. Am. Chem. Soc.* **2018**, *140*, 2363−2372.

(48) Behler, J. First Principles Neural Network Potentials for Reactive Simulations of Large Molecular and Condensed Systems. *Angew. Chem., Int. Ed. Engl.* **2017**, *56*, 12828−12840.